Realizing a spatially correlated lattice interferometer

Peng Peng,[1,*] Dekai Mao,[1,*] Yi Liang,[1] Guoling Yin,[1] Hongmian Shui,[1] Bo Song,[2,3,4,†] and Xiaoji Zhou[1,5,‡]

[1]*State Key Laboratory of Advanced Optical Communication System and Network, School of Electronics, Peking University, Beijing 100871, China*

[2]*State Key Laboratory for Mesoscopic Physics and Frontiers Science Center for Nano-optoelectronics, School of Physics, Peking University, Beijing 100871, China*

[3]*Peking University Yangtze Delta Institute of Optoelectronics, Nantong, China*

[4]*Collaborative Innovation Center of Extreme Optics, Shanxi University, Taiyuan, China*

[5]*Institute of Carbon-based Thin Film Electronics, Peking University, Shanxi, Taiyuan 030012, China*

(Received 21 January 2025; revised 19 May 2025; accepted 20 October 2025; published 12 November 2025)

Atom interferometers provide a powerful tool for measuring physical constants and affirming fundamental physics with unprecedented precision. The sensitivity of atom interferometers is significantly enhanced by optical lattices and coherent atomic sources. However, their interplay gives rise to additional complexities and intriguing phenomena. Here, we report on realizing a Ramsey-Bordé interferometer of coherent matter waves modified by a moving optical lattice in a gravitational field, and explore a resulting multipath interference with tunable coherence. We investigate spatial correlations of atoms both within the lattice and between two arms by interferometry, and observed the emerging multiple interference peaks of the Bose-Einstein condensate with sublattice site resolution. Our findings agree well with simulations, paving the way for high-precision interferometry and exploring rich interferometer phenomena using ultracold atoms.

DOI: 10.1103/htfk-k752

I. INTRODUCTION

Atom interferometry is a high-precision method for probing physical quantities and affirming fundamental physics, ranging from inertial sensing, gravitational wave detection, ultralight dark matter, and dark energy search, to testing the Standard Model and quantum mechanics in new regimes [1–10]. The sensitivity of atom interferometers is limited by the enclosed space-time area. Enhancing this area requires increasing interrogation time and the separation between the interferometer arms. Recent advances in atom interferometers with optical lattices substantially increased the interrogation time by holding atoms, leading to considerable enhancement in detection sensitivity [11,12]. Meanwhile, coherent atomic sources such as Bose-Einstein condensates (BECs) exhibited long-range phase coherence, enabling larger momentum transfers, greater arm separations in interferometry, as well as quantum-enhanced measurements [13–21].

Here we report on a spatially correlated interferometer with coherence-tunable matter waves modified by an optical lattice along gravity. We achieve a momentum transfer of 118 photon recoils while maintaining high interference contrast using Bloch oscillations in optical lattices. We investigate the effect of coherence on both the interference of atoms in two arms and the interference of atoms between neighboring sites within the lattice in the same arm, termed "intraference." We observe the emerging multipath interference due to the long-range coherence feature of the BEC, and study the amplitude change and position shift of the interference contrast. "Intraference" and interference between two arms together give rise to a multipath interference. We further precisely measure the correlation of atoms in the optical lattice. Our interferometry with the flight time of around 200 ms here provides more accurate spatial correlations. Finally, we highlight that the detection time is important for a novel open atom interferometer and probe the time evolution of the interference pattern.

II. ATOM INTERFEROMETER

Our atom interferometer is built upon a Ramsey-Bordé interferometer modified by a moving optical lattice. Figure 1 shows the experimental protocol of the atom interferometer in the frame of the cloud in the $|F=1\rangle$ state. Atoms are first split by a pair of $\pi/2$ Raman pulses coupling $|F=1\rangle$ and $|F=2\rangle$ states. The duration of $\pi/2$ pulses is 6 μs.After the first $\pi/2$ Raman pulse, atoms are in a coherent superposition with equal amplitudes of the $|F=1\rangle$ and $|F=2\rangle$ states, accompanied by the $|F=2\rangle$ state requiring a momentum kick of $\hbar k_{\mathrm{R}}$ along the z direction (the opposite direction of gravity). Here $\hbar$ is the reduced Planck's constant and k_{R} is the effective wave number resulting from two counterpropagating Raman beams. Similarly, half of the atoms in the $|F=2\rangle$ state will return to the $|F=1\rangle$ state, with a momentum transfer $-\hbar k_{\mathrm{R}}$ after the second $\pi/2$ Raman pulse. The duration between two Raman pulses is T_{R1}. Therefore, two split atomic clouds in the $|F=1\rangle$ state are separated along the z direction with a distance $\Delta L_1 = v_{\mathrm{rec}} T_{R1}$, where the atomic recoil velocity is

*These authors contributed equally to this work.
†Contact author: bsong@pku.edu.cn
‡Contact author: xjzhou@pku.edu.cn

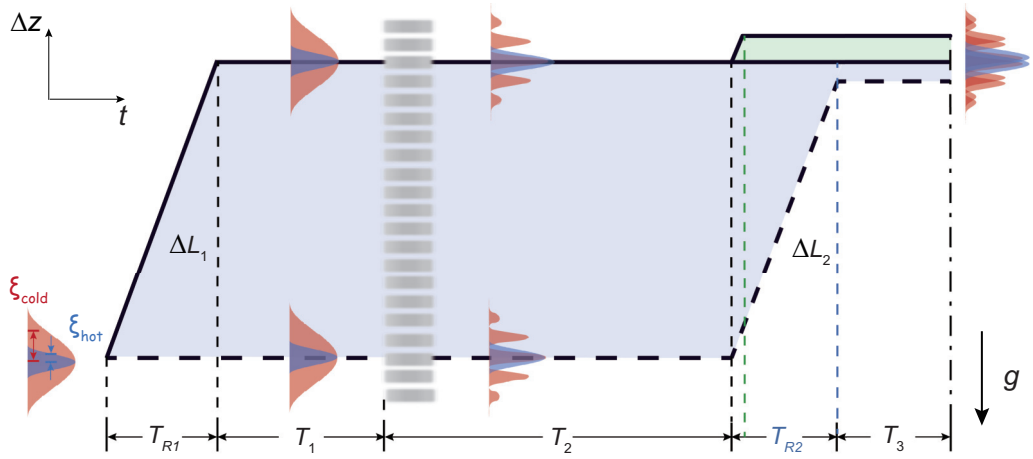

FIG. 1. Space-time representation of the atom interferometer. The atom interferometer is based on a Ramsey-Bordé interferometer modified by a moving optical lattice. Two arms of the interferometer (solid and dashed lines indicate the upper and lower arms, respectively) are split by a pair of $\pi/2$ Raman pulses separated by T_{R1}, and recombined by another pair separated by T_{R2}. Two arms are thus separated by $\Delta L_1 = v_{\rm rec} T_{R1}$ after the first pair, and atoms spaced by $\Delta L_2 = v_{\rm rec} T_{R2}$ can meet after the second pair. In between two pairs, atoms freely fall for T_1 before being loaded into a moving lattice (gray), followed by lattice unloading and an extra T_2 free fall. The interference pattern is detected (dashdotted line) after the last free fall for T_3. Red and blue indicate cold and hot atoms, respectively, and areas show the correlation with a coherence length of ξ. Horizontal and diagonal lines represent $|F = 1\rangle$ and $|F = 2\rangle$ states, respectively. The light blue area indicates the spacetime of the interference between the upper and lower arms, and the light green area indicates the interference within the optical lattice, which is termed "intraference." The blue and green dashed lines represent the final Raman $\pi/2$ pulse for those two cases.

$v_{\rm rec} = \hbar k_{\rm R}/m_{\rm Rb}$. Atoms in the undesired $|F = 2\rangle$ state in both arms are removed by a near-resonant light.

Atoms are then loaded into a moving lattice along the vertical direction in 1 ms and remain stationary with respect to the lattice frame by fine-tuning the frequency difference between the two lattice beams to compensate the gravity and achieve a net zero vertical force on the atoms. Bloch oscillations are induced by setting the relative frequency of the standing wave fields to zero along the opposite of the gravity. Then atoms are held in the lattice for extra 6 ms, during which two atomic clouds undergo 59 Bloch oscillations, i.e., $118\hbar k_L$ momentum transfer along the opposite direction of gravity. $k_L = 2\pi/\lambda_L$ is the wave number of the lattice beam with the wavelength λ_L. The integer number of Bloch oscillation cycles is chosen to ensure that the atoms return to zero quasimomentum. Bloch oscillations are stopped by tuning down the frequency difference to just compensate the gravity. Atoms are then unloaded from the lattice by ramping down the lattice depth in 1ms, followed by expanding for T_2 before the second pair of Raman pulses. The second pair recombines two arms and the interval between pulses T_{R2} determines the shift between two clouds, $\Delta L_2 = v_{\rm rec} T_{R2}$. Atomic clouds are detected after the last free fall for T_3. In our experiment, both the upper and lower arms of the interferometer are modified by the lattice, causing the atomic cloud in each arm to split into multiple paths. These paths can interfere either within the same arm or between the two arms, depending on the values of ΔL_1 and ΔL_2. For example, when $\Delta L_1 = 30d$ and $\Delta L_2 \sim d$ with the lattice spacing $d = \lambda_L/2$, only within the same arm, a phenomenon we refer to as "intraference." In contrast, when $\Delta L_2 \sim \Delta L_1$, spatial interference arises between the upper and lower arms. The total flight time is around 200 ms after atoms are released from the lattice.

III. INTERFERENCE AND INTRAFERENCE

Figure 2 shows a representative Ramsey-Bordé interference pattern and extracted contrasts for different types of lattice loading. The transition probability $\mathcal{P} = N_2/(N_1 + N_2)$ is measured as a function of the two-photon detuning of the second pair of Raman pulses δ, reflecting the phase change of the interference, where N_1 and N_2 are the numbers of atoms in $|F = 1\rangle$ and $|F = 2\rangle$ states, respectively. The contrast of the oscillatory transition probability, $\mathcal{C}$ reflects the coherence of the system. Ramsey-Bordé fringes have a background around the resonance, arising from the splitting of atoms by Raman pulses, in agreement with our theoretical simulation (solid lines; see Appendices). We first study the interference only involving atoms in different lattice sites within the same arm, i.e., "intraference" in Fig. 2(b). The extracted contrast is plotted as a function of ΔL_2, reflecting spatial coherence. Atoms in different sites evolve differently in phase due to the gravitational potential, yielding different interference patterns. We explore the impact of coherence on the fringes by varying the temperature of atoms. When the temperature is hot ($T = 540$ nK), the contrast is almost zero, indicating a very short coherence length. The critical temperature is $T_c \simeq 152$ nK. With decreasing the temperature ($T = 150$ nK), the contrast increases and the emergence of the peak at $\Delta L_2/d \approx 1$ indicates the nearest-neighbor interference. When atoms are further cooled down ($T = 50$ nK), atoms become a condensate and more peaks become visible when ΔL_2 is around an integer number of the lattice spacing as $\Delta L_2/d \approx n$. The nth peak indicates the interference between atoms spaced by nd, showing the range of the coherence. The behavior of multipeak interference manifests the long-range coherence feature of the BEC. The distance between the upper and lower arms is greater than the

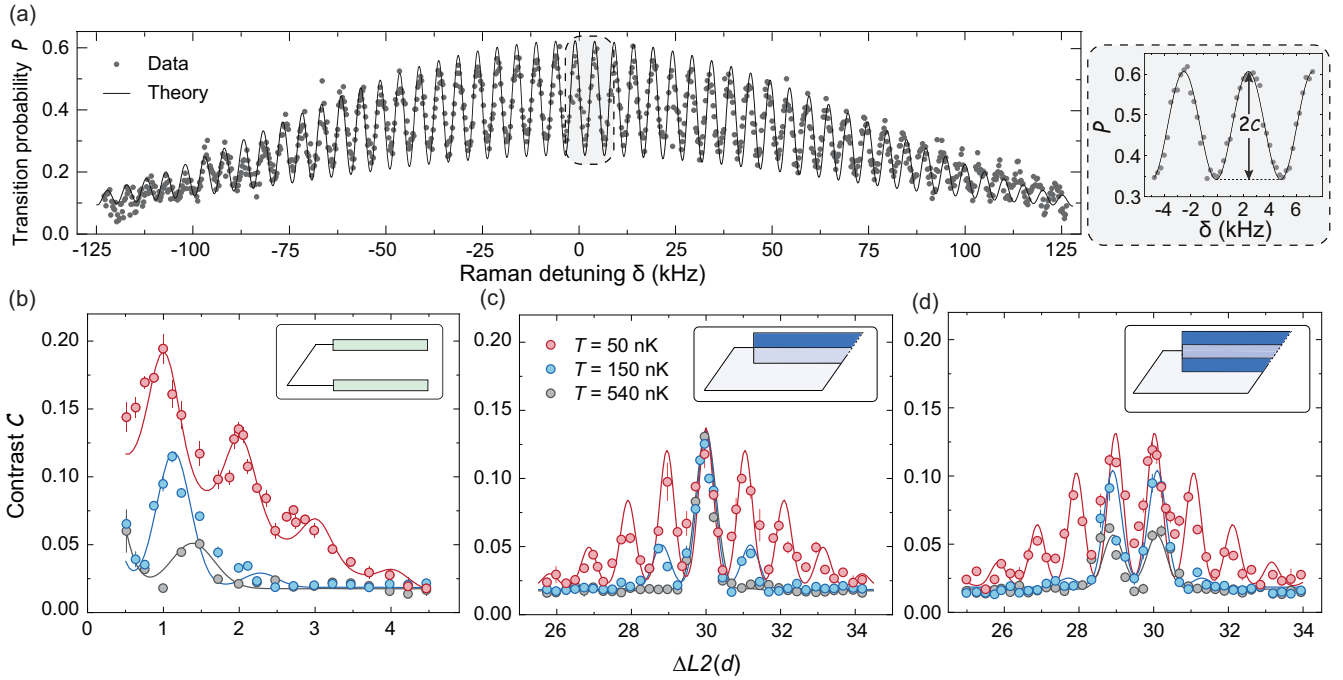

FIG. 2. Interference fringes and contrast. (a) Representative Ramsey-Bordé fringes with atoms modified by a moving optical lattice with $\Delta L_1 = \Delta L_2 = 6d$ ($T_{R1} = 198\,\mu$s) and $T = 50$ nK. The transition probability $\mathcal{P}$ oscillates with the Raman detuning δ, from which the contrast $\mathcal{C}$ is extracted. (b)–(d) Contrast of interference fringes as a function of ΔL_2 for a fixed ΔL_1. Data points are the average over three repetitions, and solid lines are simulations. Noticeable peak shifts away from integer lattice spacings are governed by the coherence length and the momentum distribution of atoms. Coherence lengths used in the simulation are $3.8d$, $1.7d$, and $1.0d$ for $T = 50$ nK, 150 nK, and 540 nK, respectively. (b) For $\Delta L_1 = 30d \gg \Delta L_2$, two arms are not recombined and only the "intraference" can exist. For $\Delta L_2 = nd$, atoms separated by nd interfere. With decreasing temperature, the coherence length becomes longer, resulting in a higher contrast of the interference and more visible interference peaks. (c) For $\Delta L_1 \approx \Delta L_2$, two arms are recombined within the coherence length. For the integer lattice loading with $\Delta L_1 = 30d$ ($T_{R1} = 993\,\mu$s), an interference peak occurs at $L_2 = L_1$. Similarly, more peaks become visible for lower temperatures. (d) For the half-integer lattice loading with $\Delta L_1 = 29.5d$ ($T_{R1} = 977\,\mu$s), where the two arms are mismatched in space, a double-peak pattern can occur even for hot atoms. Insets in (b)–(d) indicate the type of interference, and green for "intraference" only and blue for interference.

coherence length, so the final pattern should be the sum of the intraference patterns of the upper and lower arms, rather than the interference between the upper and lower arms.

However, the upper and lower arms can interfere by varying the time between Raman pulses. The contrast of interference is observed within the coherence length for $\Delta L_2 = \Delta L_1$. Atoms in different lattice sites can also form a series of subinterferometers within the coherence range, resulting in a multiple path interference. It is worth noting that the multiple path is an alternative way to improving the precision of the interferometer sensitivity by effectively narrowing down the width of fringes [22–27]. We study the condition when ΔL_1 is an integer number of the lattice spacing. Similarly, for high temperatures, the only visible peak is at $\Delta L_2 = \Delta L_1$, which reflects the fast decay of correlations in space. With decreasing the temperature, higher-order peaks up to the fourth order can be resolved at $T = 50$ nK in Fig. 2(c), manifesting the long-range coherence of the BEC. In contrast to the integer lattice loading, half-integer lattice loading, $\Delta L_1 = (n + 1/2)d$, can have a double-peak pattern when the two waves have different phases and thus destruct in the middle of two peaks. Similarly, a multiple-peak feature can appear when the matter wave has a longer coherence length, e.g., $T = 50$ nK in Fig. 2(d).

IV. SHIFT OF INTERFERENCE PEAKS

Notably, the temperature not only affects the amplitude of interference peaks but also modifies their positions. When the temperature is increased, the peaks shift outwards away from the original lattice in the "intraference" in Fig. 2(b). This effect has also been observed in the interference for both integer and half-integer lattice loading [Figs. 2(c) and 2(d). We extract the positions of interference peaks by fitting a multiple Gaussian curve to data (see Appendices).

Figure 3 shows the temperature-dependent shift of the peak, attributed by the interplay between the coherence and the spread of the atomic cloud. The larger shift in the contrast peak at higher temperatures arises from the increased spatial expansion of the atomic wave packet. Initially, the atomic wave function acquires a spatial modulation with periodicity set by the lattice constant. During subsequent free evolution, the wave function expands, and the spacing gradually increases. At higher temperatures, the broader initial momentum distribution enhances this expansion, resulting in a more pronounced increase in the spatial period over the same evolution time, and thus a larger shift in the contrast peak. The colder atomic cloud has a longer coherence length [red in Fig. 3(a)] and a narrower momentum distribution. We find that the coherence is mainly determined by the temperature.

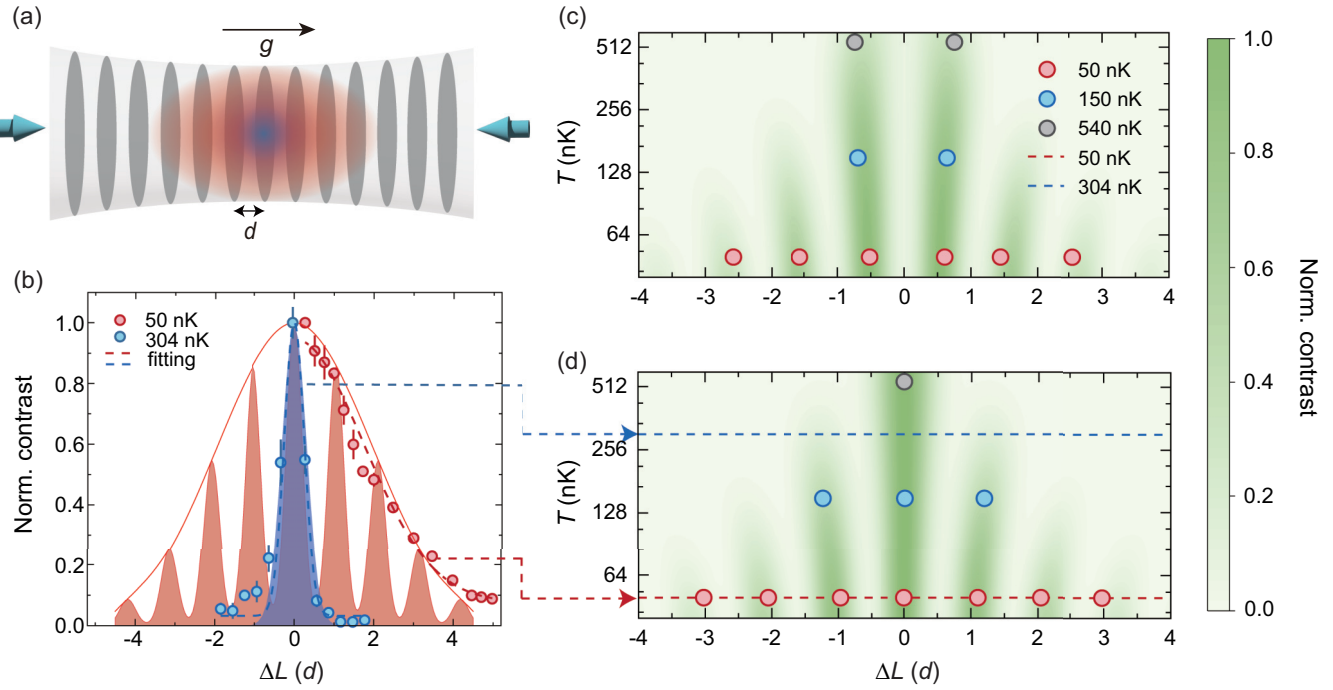

FIG. 3. Temperature-dependent shift of the contrast peak. (a) Schematic shows the correlations of atoms between different sites in an optical lattice for different temperatures. Atoms with a colder temperature (red) have a longer coherence length ξ than a hotter temperature (blue). (b) Normalized correlation of atoms as a function of the distance, $\Delta L = \Delta L_2 - \Delta L_1$ for hot atoms (blue, $T = 304\,\mathrm{nK}$) and cold atoms (red, $T = 50\,\mathrm{nK}$). The open circles and dashed lines are normalized contrasts of fringes without lattices and the fitting of the contrast using Eq. (S8) (see Appendices) for different temperatures. The filled areas are calculated correlations of atoms modified by an optical lattice, and its envelope (solid lines) matches with the correlations of atoms without lattices. (c), (d) The contrast for half-integer lattice loading with $\Delta L_1 = 29.5d$, and integer lattice loading with $\Delta L_1 = 30d$, respectively. The green background is a simulation and filled circles are the peak positions extracted from Figs. 2(c) and 2(d).

We measure the contrast of atoms without the optical lattice [open circles in Fig. 3(b)], and the measured contrast agrees well with the envelope of simulated correlations of atoms modified by the lattice. The hotter atoms (blue) have a shorter coherence length and its correlation function quickly decays with increasing the distance. Extracted peaks' positions agree well with the simulation (green) for both half-integer and integer lattice loading in Figs. 3(c) and 3(d).

V. TIME-EVOLVING INTERFERENCE OF OPEN ATOM INTERFEROMETERS

In contrast to closed atom interferometry where interference patterns are independent of the detection time, we observe the time evolution of the interference pattern for the half-integer lattice loading, a novel open atom interferometer. The upper and lower clouds modified by the optical lattice are mismatched by half a lattice spacing along gravity when two clouds meet. They evolve asynchronously due to different gravitational potentials, resulting in an evolving interference pattern. We explore this phenomenon by effectively varying the time between the last $\pi/2$ pulse and the detection, and highlight when the detection is conducted is also important for atom interferometers.

Atoms in the upper arm are split into subpaths after the lattice loading and interfere with atoms in the lower arm, respectively, forming two adjacent interferometers marked as "out" and "in." Figure 4(a) shows the accumulated phase (in the shaded rectangular) between the splitting and recombining steps $(T_2 + T_{R2})$ in light blue and gray areas, respectively, and the time before the detection T_3 in the light green area. The phases difference of two adjacent atomic interferometers are $\Delta\Phi_{\mathrm{out}}$ and $\Delta\Phi_{\mathrm{in}}$, respectively. The differential phase $\Delta\Phi_{\mathrm{diff}} = \Delta\Phi_{\mathrm{out}} - \Delta\Phi_{\mathrm{in}} = mgd\tau/\hbar$ reflects the actual phase between two interferometers. The phase of the interference, reflected by the contrast, is independent of when the last pair of Raman pulses as long as the time between the lattice loading and detection is fixed. The contrast oscillates with the total time $\tau = T_2 + T_{R2} + T_3$ (open circles) indicating the change of the phase, whereas the contrast remains constant (open squares) for a fixed τ in Fig. 4(b). Here τ is around 200 ms and the temperature of atoms is $T = 150\,\mathrm{nK}$. This multipath interference is different from conventional atom interferometers, providing a more precise way for probing nonuniform fields. A similar effect with cold atoms in an optical lattice has been observed in Ref. [11]. Our findings show that the time of the detection is critical for the atom interferometer when the matter wave is coherent in particular.

VI. CONCLUSIONS

We realize a novel Ramsey-Bordé interferometer with coherence-tunable matter waves modified by a moving optical lattice. We observe the emerging multiple interference peaks due to the long-range coherence of the BEC, and study the amplitude and shift of those peaks at different temperatures.

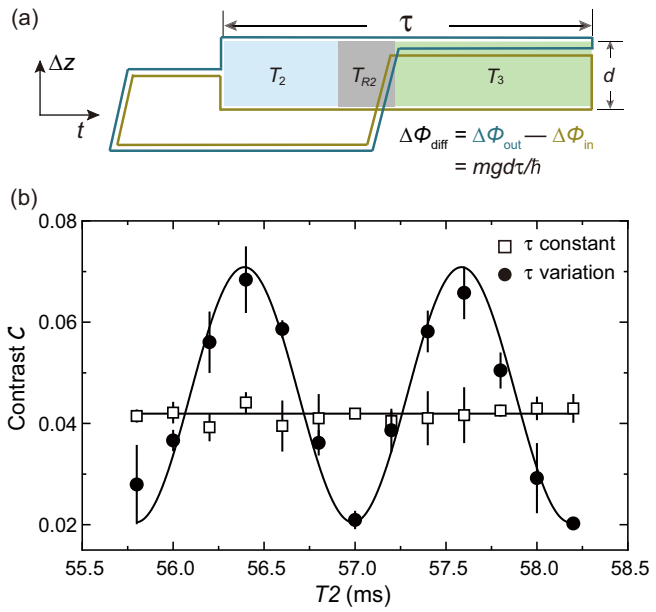

FIG. 4. Time-evolving interference of an open atom interferometer (a) The phase evolution of the atom interferometer for half-lattice loading. Two subpaths separated by a lattice spacing d of the upper arm can both interfere with the lower arm, leading to the phase of the interference evolving with time. The spacing can be tuned by the difference between ΔL_1 and ΔL_2. The shaded areas represent the differential interference phase between two paths, which is proportional to the space-time area $S = \tau d$ with the time between the lattice loading and the detection, τ. The illustration shows the relationship between the phase difference $\Delta\Phi_{\text{diff}} = \Delta\Phi_{\text{out}} - \Delta\Phi_{\text{in}}$ and the durations T_2, T_3. (b) The contrast of the fringes is plotted as a function of T_2 for the half-integer lattice loading using parameters of $(\Delta L_1, \Delta L_2) = (29.5d, 29.5d)$ at $T = 150\,\text{nK}$ for fixed (squares) or varying (circles) τ. Solid lines are linear and sinusoidal fits respectively. The phase of the interference is reflected by the contrast of the fringes. It remains almost constant (squares) for a fixed τ, whereas it oscillates with τ in a period of 1.2 ms (circles). T_3 is around 166 ms for both cases. They together show that the interference pattern not only relies on the time before the recombination of two arms, $(T_2 + T_{R2})$ but also when the interference pattern is detected T_3.

We further demonstrate precise measurements of spatial correlations for different temperatures and lattice loading using interferometry, and reveal the importance of the detection time for open atom interferometers. Our findings bridge the gap between coherent matter waves and lattice interferometry, opening the door for high-precision interferometry and intriguing interferometer phenomena.

ACKNOWLEDGMENTS

This work was supported by National Key Research and Development Program of China (Grants No. 2021YFA0718300 and No. 2021YFA1400900) and the National Natural Science Foundation of China (Grants No. 92365208 and No. 11934002). B.S. acknowledges support from the Natural Science Foundation of China (Grant No. 12374242), the Innovation Program for Quantum Science and Technology (Grant No. 2024ZD0301800) and the Beijing Natural Science Foundation (Grant No. Z240007).

DATA AVAILABILITY

The data that support the findings of this article are openly available [28].

APPENDIX A: EXPERIMENTAL SETUP AND SEQUENCE

Our experiments begin with preparing cold atoms or a BEC of around 1.5×10^5 ^{87}Rb atoms in the $|F = 1, m_F = 0\rangle$ state. Here F denotes the total angular momentum and m_F the magnetic quantum number of the state. The temperature of the atoms is in a range from $T = 50\,\text{nK}$ to 540 nK by adjusting the final power of the crossed optical dipole trap (CODT) at the end of evaporative cooling. Next, atoms are suddenly released from the trap, fall freely along gravity, and enter the interferometer.

Then atoms are split by Raman coupling and have different momenta, leading to different atomic trajectories. The Raman coupling consists of Raman 1 ($R1$) and the retroreflected Raman 2 ($R2$), with the Doppler shift preventing resonant coupling between $R1$ and the incident $R2$. The Raman beam is red-detuned by 825 MHz from the atomic resonance. The two-photon Raman transition couples the $|F = 1\rangle$ and $|F = 2\rangle$ states, resulting in a momenta transfer, $\hbar k_{\text{R}}/m_{\text{Rb}} = 11.8\,\text{mm/s}$ where k_{R} is the effective wave number resulting from two counterpropagating Raman beams. Four $\pi/2$ Raman pulses are used to split and recombine atomic clouds for creating the atom interferometer. The $R2$ beam and its retroreflected beam form an optical lattice, causing around 10% of the atoms in the $|F = 1\rangle$ state to be scattered upward and downward due to Kapitza-Dirac diffraction, with the Doppler shift of the atoms already taken into account. Atoms scattered downward do not affect the interference, whereas those scattered upward $|F = 1\rangle$ can mix with $|F = 2\rangle$. However the recoil velocities are nearly identical for both the $R1$-$R2$ pair and the scattering from the $R2$ lattice. And our clean beams remove these unwanted $|F = 2\rangle$ atoms after the second Raman pulse in Fig. 7. Therefore, this scattering contributes to the infidelity of the Raman pulses ($R1$ and $R2$) and reduces the fringe contrast, but has minimal effect on the interference phase.

The wavelength of the moving optical lattice is $\lambda_{\text{lat}} = 780\,\text{nm}$, blue-detuned by 45 GHz from the $|5^2S_{1/2}, F = 1\rangle \rightarrow |5^2P_{3/2}, F' = 0\rangle$ transition, and the lattice constant is $d = \lambda_{\text{lat}}/2 = 390\,\text{nm}$. Atoms are initially prepared at quasimomentum $q = 0$. The frequency difference between the two lattice beams is optimized during lattice loading and unloading so that the atoms remain relatively stationary with the lattice.

The lattice depth is linearly ramped up over a duration of 1 ms, while the frequency detuning between the counterpropagating lattice beams is scanned by $2\pi \times 12.6\,\text{kHz}$ to match the initial atomic velocity. This comoving configuration ensures that the lattice velocity follows the atomic motion during the ramp, avoiding any sudden momentum change. As a result, the atoms remain in the same quasimomentum state throughout the process, and no interband excitations are observed.

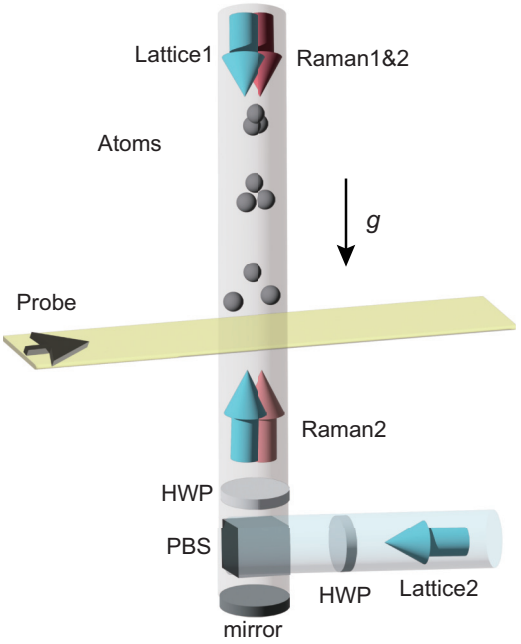

FIG. 5. Experimental setup. Cold rubidium atoms fall freely from a moving optical lattice (cyan arrows) along the gravity direction. The moving lattice consists of two counter-propagating beams with a tunable frequency difference. Raman pulses (pink arrows) are used to split and recombine atomic clouds. Two Raman beams are shined from the top, rotated by a half-wave plate (HWP) and retroreflected by the mirror at the bottom. The upper Raman beams has two linearly polarized light and they are orthogonal. One of them is filtered out by the PBS and the other one is reflected upwards. The probe beam is shined perpendicular to the gravity direction for detecting the interference pattern.

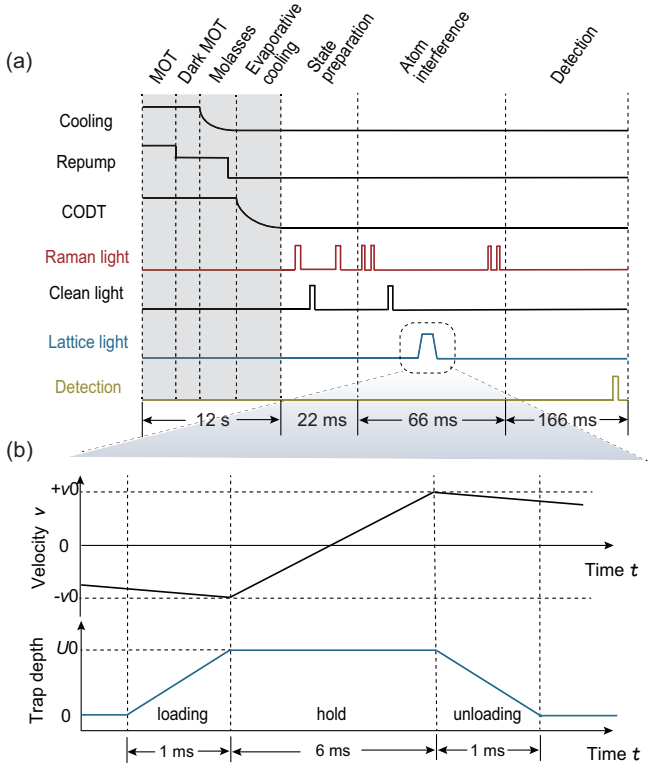

FIG. 6. The experimental sequence. (a) The sequence consists of the preparation of atoms (shaded grey area) and the atom interferometry (white area). (b) A zoomed-in sequence of the moving lattice. The upper and lower figures show the velocity change of the moving lattice and the trap depth. The velocity is controlled by tuning the frequency difference between the two lattice beams during lattice loading and unloading to ensure that the atoms remain relatively stationary with respect to the moving lattice.

The time of lattice loading is 1 ms. The adiabatic criterion of lattice loading can bemet as $|\frac{d}{dt}U_0/E_R| \ll 32\sqrt{2}E_R/\hbar$ and the loading time satisfies this criterion [29]. The hold time in the optical lattice is 6 ms, during which atoms undergo 59 Bloch oscillations. After the lattice unloading within 1 ms, atoms are released from the lattice. Figures 5 and 6 show the experimental setup and the sequence, respectively.

APPENDIX B: ATOM INTERFEROMETRY

The Ramsey-Bordé interferometer consists of two pairs of Raman pulses to split and recombine the atomic cloud, shown in Fig. 1 in the main text. The first $\pi/2$ pulse induces a superposition between the $|F = 1\rangle$ state and the $|F = 2\rangle$ state of ^{87}Rb atoms [30]. The transferred atoms in the $|F = 2\rangle$ state obtain the extra momenta induced by the Raman transition and move upwards with respect to the original $|F = 1\rangle$ state.

After the first pair of Raman pulses, the two arms of the interferometer are in the same hyperfine state and momentum, $|F = 1, p = p_0\rangle$, whereas atoms in the unwanted arms, $|F = 2, p = p_0 + \Delta p\rangle$ are removed by a clean beam on resonance of the $|F = 2\rangle \rightarrow |F' = 3\rangle$ transition. Atoms in two arms fall freely and remain relatively stationary with respect to the lattice frame along the gravity direction during lattice loading and unloading. The frequency difference between the two lattice beams is scanned at 25.1 MHz/s to compensate the chirp rate of the Doppler frequency shift caused by the gravity. Atoms gain momentum transfer during Bloch oscillations in the moving lattice [31] and are coherently kicked upwards by the lattice. This kick effect can be used to fold the trajectory and acquire a longer evolution time for the interferometer to achieve higher sensitivity in a limited space [32].

After atoms are unloaded from the lattice for 50 ms, we apply the second pair of Raman pulses. In the experiment, the Raman coupling is detuned by δ from the resonance in the second pair of Raman pulses. We scan the Raman detuning, δ in the experiment and measure the transition probability, $\mathcal{P}$ in Fig. 2(a) in the main text.

APPENDIX C: INTERFERENCE FRINGE

We simulate fringes of the atom interferometer using a semi-classical method based on the phase and weight of the wave functions along interferometer paths shown in Fig. 7. The Raman transfer coefficient relies on the detuning δ, $\alpha = (\Omega/\sqrt{\Omega^2 + \delta^2})\sin(t_L\sqrt{\Omega^2 + \delta^2}/2)$, where Ω is the Rabi frequency and t_L is the pulse duration, and the rest state is thus $\beta = \sqrt{1 - \alpha^2}$.

The initial weight of each wave function is equally split from the same cloud and thus has a factor of $\sqrt{2}/2$. After two

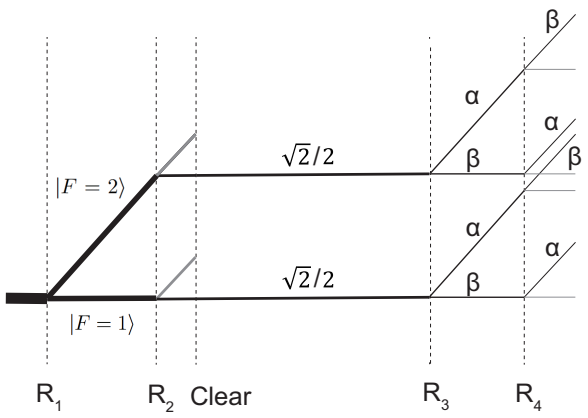

FIG. 7. The weight change of atomic wave functions along the interferometer paths. Weights of wave functions are marked after Raman pulses along the interferometer paths. R_1-R_4 and Clear denote the Raman pulses and the cleaning pulses of removing the $|F = 2\rangle$ state, respectively. Gray lines indicate paths which are not involved in the atom interfereometer.

Raman pulses, two paths of the $|F = 2\rangle$ state at the output port of the interferometer read

$$\psi_1 = \frac{\sqrt{2}}{2}\alpha\beta e^{i\phi_c},$$
$$\psi_2 = \frac{\sqrt{2}}{2}\alpha\beta e^{i(\phi_c+\phi_d)}, \tag{C1}$$

where ϕ_c is the common phase for the two wave functions, and the differential phase $\phi_d = T_R\delta + \phi_0$ with ϕ_0 being the offset. The probability of the $|F = 2\rangle$ state is

$$\mathcal{P} = |\psi_1 + \psi_2|^2 + \frac{\sqrt{2}}{2}\alpha\beta \times 2, \tag{C2}$$

where the last term from the other two diverging paths of the $|F = 2\rangle$ state only contributes an offset to the fringe, as it exceeds the coherence length of ψ_1 and ψ_2 (see Fig. 7). The above interference fringe $\mathcal{P}$ is plotted as the function of δ in Fig. 2(a) in the main text, where a fudge factor of 0.49 is multiplied and an offset of 0.07 to count the imperfect Raman transition and detection in the simulation.

APPENDIX D: PHASE OF THE INTERFEROMETER

The accumulated phase of the atom interferometer $\Delta\Phi = \Delta\Phi_{\text{Prop}} + \Delta\Phi_{\text{Laser}}$ consists of the propagation phase $\Delta\Phi_{\text{Prop}}$ and the laser phase $\Delta\Phi_{\text{Laser}}$. $\Delta\Phi_{\text{Prop}}$ is proportional to the integration of Lagrangian, contributed to by the kinetic energy and the potential energy

$$\Delta\Phi_{\text{Prop}} = \frac{1}{\hbar}\int_{t_0}^{t_d}\left(\frac{1}{2}mv_{\text{up}}^2 - \frac{1}{2}mv_{\text{low}}^2\right)dt - \frac{mg}{\hbar}\int_{t_0}^{t_d}(z_{\text{up}} - z_{\text{low}})\,dt, \tag{D1}$$

where the subscripts "up" and "low" indicate upper and lower arms, respectively, t_0 and t_d is the time of the first Raman pulse and the detection time, respectively. The laser phase $\Delta\Phi_{\text{Laser}}$ is determined by the time and the position of the laser beam

$$\Delta\Phi_{\text{Laser}} = \Phi_1 - \Phi_2 - \Phi_3 + \Phi_4,$$
$$\Phi_i = k_{\text{eff}}z_i - \int_{t_0}^{t_i}\omega_R\,dt, \tag{D2}$$

where z_i denotes the position at which atoms interact with the ith Raman pulse, and ω_R is the Raman frequency, which is chirped to compensate for the Doppler frequency shift of free-falling atoms. The $+/-$ sign before Φ_i indicates the direction of the Raman transition from the state $|F = 1\rangle$ to $|F = 2\rangle$ or $|F = 2\rangle$ to $|F = 1\rangle$, respectively. Since $\Delta\Phi_{\text{Laser}}$ is the differential phase between two arms, phases accumulated from the optical lattice are canceled out, whereas the one from four Raman pulses remains.

The phase difference of interferometers induces the differential phase between different interferometers. The phase difference for two interferometers in Fig. 4(a) are $\Delta\Phi_{\text{out}}$ and $\Delta\Phi_{\text{in}}$, giving rise to a beat when scanning the differential phase

$$\Delta\Phi_{\text{diff}} = \Delta\Phi_{\text{out}} - \Delta\Phi_{\text{in}} = \frac{mgd}{\hbar}\tau, \tag{D3}$$

where the inhomogeneity of the gravity is ignored. Thus the space-time area is a rectangle enclosed by the two arms in Fig. 4(a) in the main text.

APPENDIX E: CONTRAST OF THE INTERFERENCE

The fringe contrast is determined by the coherence of the system and the atomic distribution. The coherence length along the lattice direction is estimated using the interference of two arms [33]. We assume the wave function in one arm as the integral of plane waves over the momentum p,

$$\psi(z) = \frac{1}{(\sqrt{2\pi}\sigma_p)^{1/2}}\int e^{-\frac{p^2}{4\sigma_p^2}}e^{\frac{i}{\hbar}(pz-\frac{p^2}{2m}t)}\,dp, \tag{E1}$$

where the standard deviation σ_p of the momentum distribution along the gravity direction is estimated by the equipartition theorem $\sigma_p^2/m = k_BT$. The other arm of the interferometer can be written as $\psi(z - \delta L)e^{i\phi_m}$, where δL is the space between two arms, and ϕ_m is the accumulated phase from different paths and laser pulses. Therefore, the overall probability is the integration over the z direction

$$P_{\delta L} = \frac{1}{4}\int|\psi(z) + \psi(z - \delta L)e^{i\phi_m}|^2\,dz = \frac{1}{2} + \frac{1}{2\sqrt{2\pi}\sigma_p}\int e^{-\frac{p^2}{2\sigma_p^2}}\cos\left(\frac{p}{\hbar}\delta L + \phi_m\right)dp. \tag{E2}$$

The fringe contrast $\mathcal{C}$ reads

$$\mathcal{C}(P_{\delta L}) = \frac{1}{2\sqrt{2\pi}\sigma_p}\int e^{-\frac{p^2}{2\sigma_p^2}}\cos\left(\frac{p}{\hbar}\delta L\right)dp \approx \mathcal{C}_0 + Ae^{-\frac{2\delta L^2}{\xi^2}}, \tag{E3}$$

where $\mathcal{C}_0$ and A are the offset and amplitude, respectively. The extracted coherence length is determined as $\xi = 2\hbar/\sigma_p$ when σ_p approaches zero [33,34].

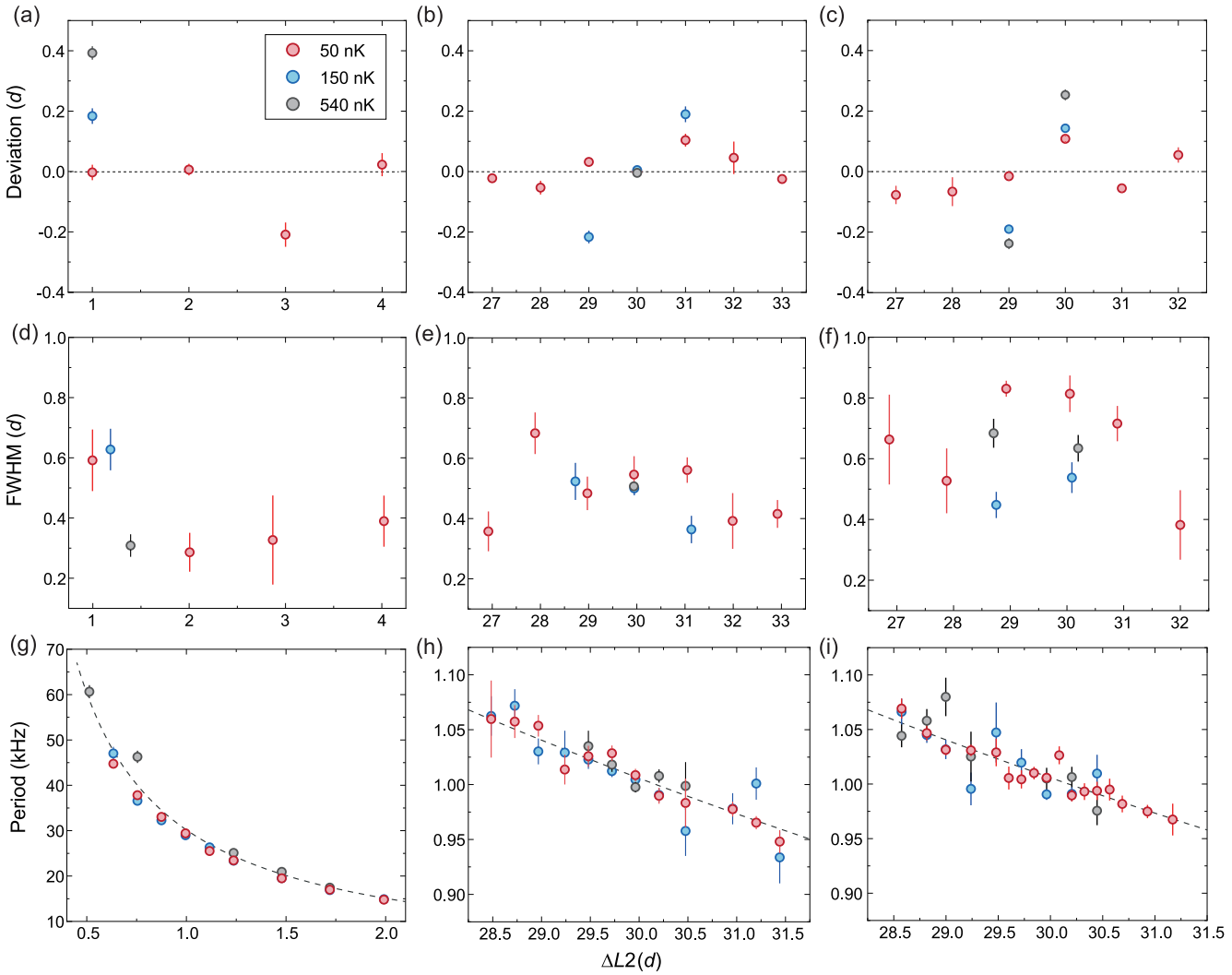

FIG. 8. Characteristics of multiple peaks. Position deviation, full width at half maximum (FWHM) and fringe periods of multiple peaks for different temperatures are extracted by fitting voigt curves to the data in Fig. 2 in the main text. (a), (d), (g), (b), (e), (h), and (c), (f), (i) are the intraference, the integer lattice loading with $\Delta L_1 = 30d$, and the half-integer lattice loading with $\Delta L_1 = 29.5d$, respectively. (a)–(c) show the shift of peaks from the lattice position and dashed lines indicate zero. The shift increases with increasing the temperature. (d)–(f) are FWHMs for different temperatures. (g)–(i) are the periods of Ramsey fringes, in good agreement with theoretical calculations (dashed lines).

In the experiment, the durations of lattice loading and unloading are chosen to be relatively short to induce the lattice modulation to the atomic cloud. For a deep lattice, $V_{\text{lat}} = 40E_r$, the overlap of maximally localized Wannier functions $w(z)$ between adjacent sites is negligible. Thus the system wave function $W(z)$ is the sum of Wannier functions

$$W(z) = \frac{1}{(\sqrt{2\pi}N)^{1/2}} e^{-\frac{z^2}{4N^2}} \sum_{z'=-4N}^{4N} w\left(\frac{z+z'}{d'/d}\right), \tag{E4}$$

where N denotes the Gaussian envelope to normalize the modulated wave function $\psi(z)W(z)$ and is set to be $10d$, much smaller than the actual size (hundreds of times d). d' denotes the modulated spacing after the expansion at the detection time. The atomic cloud is assumed to expand ballistically as $\sigma(t)^2 = \sigma_0^2 + \sigma_p^2 t^2/m^2$ with the initial spread σ_0, and we have $d'/d = \sigma(T_0 + T_{R1} + T_1 + T_2 + T_{R2} + T_3)/\sigma(T_0 + T_{R1} + T_1)$, where T_0 denotes the time interval from the cloud release to the first Raman pulse, and T_i and T_{Ri} denote the intervals between the pulse sequences in Fig. 1 in the main text. This contributes to the outward shift of the peaks in Figs. 2(b)–2(d) in the main text.

Substituting $\psi(z)$ with the modulated wave function $\psi(z)W(z)$, the modulated contrast $\mathcal{C}'(P_{\delta L})$ can be derived as follows:

$$\mathcal{C}'(P_{\delta L}) = \mathcal{C}(P_{\delta L}) \times \int W(z)W(z-\delta L)\,dz. \tag{E5}$$

For the simulations in Figs. 2(b)–2(d) in the main text, the initial size is $380\,d$, and the parameter σ_p is chosen to fit the experimental data.

APPENDIX F: ANALYSIS OF THE PEAKS

Figure 2 in the main text shows that the peak position of the fringe contrast mismatches integer lattice spacings,

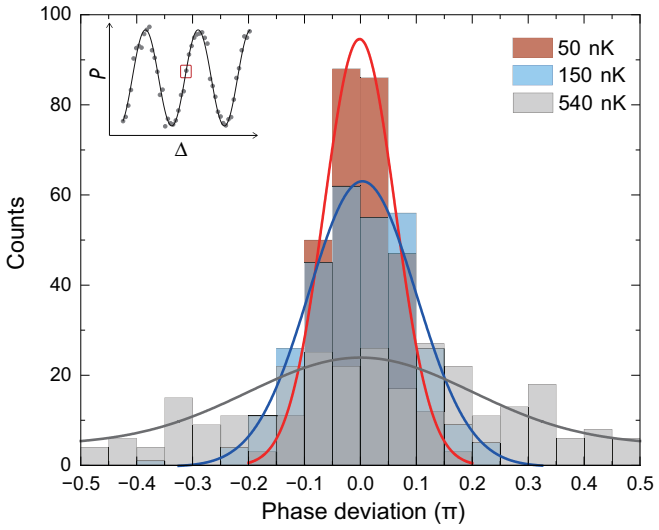

FIG. 9. Phase fluctuations. The phase fluctuation results measured with the BEC (red), impure BEC (blue), and cold atoms (gray) are presented as histograms. The solid lines represent Gaussian fitting curves, where the standard deviations are 0.063π for the BEC, 0.096π for the impure BEC and 0.20π for the cold atoms. The stability of the phase is clearly enhanced by coherent matter waves.

particularly when the coherence length becomes short. We fit a Voigt curve to the data, and extract the shift and the width of peaks in Fig. 8. The error bar indicates the standard deviation of the fitting.

Figures 8(a)–8(c) show the temperature-dependent deviation. When the temperature of atoms is cold ($T = 50\,\mathrm{nK}$), peaks align with integer lattice sites, whereas the shift becomes larger with increasing the temperature. The widths of peaks for different temperatures are extracted in Figs. 8(d)–8(f). Figures 8(g)–8(i) show the period of Ramsey spectroscopy which is extracted by fitting a sinusoidal curve to Ramsey fringes. The period of Ramsey fringes is inversely proportional to ΔL_2. Figures 8(g)–8(i) are the collapsed experimental data on the theoretical curves, and show that the period is independent on the temperature.

APPENDIX G: ENHANCED PHASE MEASUREMENT

We further study enhanced precision measurements in the interferometer using coherent atomic sources. Figure 9 presents the interference fringe point with the maximum slope, measured over 300 repetitions at three different temperatures. The chosen point is sensitive to phase fluctuations, a similar method as that used in Ref. [20]. Our phase fluctuation measurements demonstrate the enhancement offered by ultracold atoms in high-precision atomic interferometry. The standard deviation results extracted by normal distribution fits indicate that the measurement precision for the BEC is 1.5 (1.8dB) and 3.2 times (5dB) higher than that for atoms at the BEC transition and cold atoms, respectively.

we provided estimated uncertainties and their contribution to the phase accuracy below. The atom number fluctuates by approximately 10%, contributing around $3\text{–}7 \times 10^{-5}\pi$ in the phase measurement in Fig. 9. Temperature fluctuations of 10–20 nK contribute about $3\text{–}5 \times 10^{-4}\pi$, estimated by the temperature-dependent data in Fig. 3 in the main text. The imperfections in the Raman pulses, around 25%, introduce an uncertainty of roughly $4 \times 10^{-3}\pi$.

[1] A. D. Cronin, J. Schmiedmayer, and D. E. Pritchard, Optics and interferometry with atoms and molecules, Rev. Mod. Phys. **81**, 1051 (2009).

[2] S. Dimopoulos, P. W. Graham, J. M. Hogan, M. A. Kasevich, and S. Rajendran, Atomic gravitational wave interferometric sensor, Phys. Rev. D **78**, 122002 (2008).

[3] S. Dimopoulos, P. W. Graham, J. M. Hogan, and M. A. Kasevich, Testing general relativity with atom interferometry, Phys. Rev. Lett. **98**, 111102 (2007).

[4] H. Müller, S.-W. Chiow, S. Herrmann, S. Chu, and K.-Y. Chung, Atom-interferometry tests of the isotropy of post-newtonian gravity, Phys. Rev. Lett. **100**, 031101 (2008).

[5] R. H. Parker, C. Yu, W. Zhong, B. Estey, and H. Müller, Measurement of the fine-structure constant as a test of the standard model, Science **360**, 191 (2018).

[6] P. Asenbaum, C. Overstreet, M. Kim, J. Curti, and M. A. Kasevich, Atom-interferometric test of the equivalence principle at the 10^{-12} level, Phys. Rev. Lett. **125**, 191101 (2020).

[7] K. Bongs, M. Holynski, J. Vovrosh, P. Bouyer, G. Condon, E. Rasel, C. Schubert, W. P. Schleich, and A. Roura, Taking atom interferometric quantum sensors from the laboratory to real-world applications, Nat. Rev. Phys. **1**, 731 (2019).

[8] M. Abe, P. Adamson, M. Borcean *et al.*, Matter-wave atomic gradiometer interferometric sensor (MAGIS-100), Quantum Sci. Technol. **6**, 044003 (2021).

[9] L. Badurina, E. Bentine, D. Blas *et al.*, AION: An atom interferometer observatory and network, J. Cosmol. Astropart. Phys. 05 (2020) 011.

[10] M.-S. Zhan, J. Wang, W.-T. Ni *et al.*, ZAIGA: Zhaoshan long-baseline atom interferometer gravitation antenna, Int. J. Mod. Phys. D **29**, 1940005 (2020).

[11] V. Xu, M. Jaffe, C. D. Panda, S. L. Kristensen, L. W. Clark, and H. Müller, Probing gravity by holding atoms for 20 seconds, Science **366**, 745 (2019).

[12] C. D. Panda, M. J. Tao, M. Ceja, J. Khoury, G. M. Tino, and H. Müller, Measuring gravitational attraction with a lattice atom interferometer, Nature (London) **631**, 515 (2024).

[13] M. Gersemann, A. Rajagopalan, M. Abidi, P. Barbey, A. Sabu, X. Chen, N. Weddig, B. Tennstedt, J. Petring, N. Droese *et al.*, Developments for quantum inertial navigation systems employing Bose–Einstein condensates, Appl. Phys. Rev. **12**, 031306 (2025).

[14] M. Andrews, C. Townsend, H.-J. Miesner, D. Durfee, D. Kurn, and W. Ketterle, Observation of interference between two bose condensates, Science **275**, 637 (1997).

[15] Y. Shin, M. Saba, T. A. Pasquini, W. Ketterle, D. E. Pritchard, and A. E. Leanhardt, Atom interferometry with Bose-Einstein condensates in a double-well potential, Phys. Rev. Lett. **92**, 050405 (2004).

[16] I. Bloch, T. W. Hänsch, and T. Esslinger, Measurement of the spatial coherence of a trapped Bose gas at the phase transition, Nature (London) **403**, 166 (2000).

[17] X. Guo, Z. Yu, F. Wei, S. Jin, X. Chen, X. Li, X. Zhang, and X. Zhou, Quantum precision measurement of two-dimensional forces with 10^{-28}-Newton stability, Sci. Bull. **67**, 2291 (2022).

[18] V. Giovannetti, S. Lloyd, and L. Maccone, Quantum-enhanced measurements: Beating the standard quantum limit, Science **306**, 1330 (2004).

[19] J. Esteve, C. Gross, A. Weller, S. Giovanazzi, and M. K. Oberthaler, Squeezing and entanglement in a Bose–Einstein condensate, Nature (London) **455**, 1216 (2008).

[20] C. Gross, T. Zibold, E. Nicklas, J. Esteve, and M. K. Oberthaler, Nonlinear atom interferometer surpasses classical precision limit, Nature (London) **464**, 1165 (2010).

[21] R. Karcher, A. Imanaliev, S. Merlet, and F. P. D. Santos, Improving the accuracy of atom interferometers with ultracold sources, New J. Phys. **20**, 113041 (2018).

[22] G. Weihs, M. Reck, H. Weinfurter, and A. Zeilinger, All-fiber three-path Mach–Zehnder interferometer, Opt. Lett. **21**, 302 (1996).

[23] M. Weitz, T. Heupel, and T. W. Hänsch, Multiple beam atomic interferometer, Phys. Rev. Lett. **77**, 2356 (1996).

[24] H. Hinderthür, F. Ruschewitz, H.-J. Lohe, S. Lechte, K. Sengstock, and W. Ertmer, Time-domain high-finesse atom interferometry, Phys. Rev. A **59**, 2216 (1999).

[25] Z. Hadzibabic, S. Stock, B. Battelier, V. Bretin, and J. Dalibard, Interference of an array of independent Bose-Einstein condensates, Phys. Rev. Lett. **93**, 180403 (2004).

[26] M. Robert-de-Saint-Vincent, J.-P. Brantut, C. J. Bordé, A. Aspect, T. Bourdel, and P. Bouyer, A quantum trampoline for ultra-cold atoms, Europhys. Lett. **89**, 10002 (2010).

[27] J. Petrovic, I. Herrera, P. Lombardi, F. Schaefer, and F. S. Cataliotti, A multi-state interferometer on an atom chip, New J. Phys. **15**, 043002 (2013).

[28] Please see https://doi.org/10.18170/DVN/AYP8VV for the available data.

[29] M. Ben Dahan, E. Peik, J. Reichel, Y. Castin, and C. Salomon, Bloch oscillations of atoms in an optical potential, Phys. Rev. Lett. **76**, 4508 (1996).

[30] M. Kasevich, D. S. Weiss, E. Riis, K. Moler, S. Kasapi, and S. Chu, Atomic velocity selection using stimulated Raman transitions, Phys. Rev. Lett. **66**, 2297 (1991).

[31] E. Peik, M. Ben Dahan, I. Bouchoule, Y. Castin, and C. Salomon, Bloch oscillations of atoms, adiabatic rapid passage, and monokinetic atomic beams, Phys. Rev. A **55**, 2989 (1997).

[32] M. Andia, R. Jannin, F. Nez, F. Biraben, S. Guellati-Khélifa, and P. Cladé, Compact atomic gravimeter based on a pulsed and accelerated optical lattice, Phys. Rev. A **88**, 031605(R) (2013).

[33] J. Kellogg, N. Yu, J. Kohel, R. Thompson, D. Aveline, and L. Maleki, Longitudinal coherence in cold atom interferometry, J. Mod. Opt. **54**, 2533 (2007).

[34] L. P. Parazzoli, A. M. Hankin, and G. W. Biedermann, Observation of free-space single-atom matter wave interference, Phys. Rev. Lett. **109**, 230401 (2012).